UC San Diego
UC San Diego Previously Published Works

Title

The role of traction in membrane curvature generation

Permalink

https://escholarship.org/uc/item/8rp7f25b

Journal

Molecular Biology of the Cell, 29(16)

ISSN

1059-1524

Authors

Alimohamadi, H
Vasan, R
Hassinger, JE
et al.

Publication Date

2018-08-08

DOI

10.1091/mbc.e18-02-0087

Peer reviewed

The role of traction in membrane curvature generation

H. Alimohamadi[a,†], R. Vasan[a,†], J.E. Hassinger[b], J.C. Stachowiak[c], and P. Rangamani[a,*]
[a]Department of Mechanical and Aerospace Engineering, University of California, San Diego, La Jolla, CA 92093;
[b]Biophysics Graduate Program, University of California, Berkeley, Berkeley, CA 94720; [c]Department of Biomedical Engineering, University of Texas at Austin, Austin, TX 78712

ABSTRACT Curvature of biological membranes can be generated by a variety of molecular mechanisms including protein scaffolding, compositional heterogeneity, and cytoskeletal forces. These mechanisms have the net effect of generating tractions (force per unit length) on the bilayer that are translated into distinct shapes of the membrane. Here, we demonstrate how the local shape of the membrane can be used to infer the traction acting locally on the membrane. We show that buds and tubes, two common membrane deformations studied in trafficking processes, have different traction distributions along the membrane and that these tractions are specific to the molecular mechanism used to generate these shapes. Furthermore, we show that the magnitude of an axial force applied to the membrane as well as that of an effective line tension can be calculated from these tractions. Finally, we consider the sensitivity of these quantities with respect to uncertainties in material properties and follow with a discussion on sources of uncertainty in membrane shape.

INTRODUCTION

Cell shape plays an important role in regulating a diverse set of biological functions, including development, differentiation, motility, and signal transduction (McMahon and Gallop, 2005; Roux *et al.*, 2005; Neves *et al.*, 2008; Rangamani *et al.*, 2013; Aimon *et al.*, 2014). Additionally, the ability of cellular membranes to bend and curve is critical for a variety of cellular functions such as membrane trafficking processes, cytokinetic abscission, and filopodial extension (Mukherjee and Maxfield, 2000; Mattila and Lappalainen, 2008). To carry out these functions, cells harness diverse mechanisms of curvature generation such as compositional heterogeneity (Baumgart *et al.*, 2003; Römer *et al.*, 2007), protein scaffolding (Karotki *et al.*, 2011; Kirchhausen, 2012), insertion of amphipathic helices into the bilayer (Ford *et al.*, 2002; Lee *et al.*, 2005), and

forces exerted by the cytoskeleton (Giardini *et al.*, 2003; Carlsson, 2018) (Figure 1). Reconstituted and synthetic membrane systems also exhibit a wide range of shapes in response to different curvature-inducing mechanisms, as seen with steric pressure due to protein crowding (Lipowsky, 1995; Stachowiak *et al.*, 2012; Derganc and Čopič, 2016).

It is well known that these various mechanisms of curvature generation induce surface stresses; expressions for these stresses have been derived using either variational methods (Jenkins, 1977; Capovilla and Guven, 2002b, 2004) or by using auxiliary variables that enforce geometric constraints (Guven, 2004; Fournier, 2007). These studies have established the physics underlying membrane stresses and clearly explained how these traction forces can be interpreted in linear deformations and in idealized geometries (Guven, 2004; Fournier, 2007). However, many physiologically relevant membrane shapes display large curvatures (Farsad and De Camilli, 2003; Kozlov *et al.*, 2014), nonlinear deformations (Holzapfel *et al.*, 1996; Einstein *et al.*, 2003), and heterogeneous membrane composition (Lingwood and Simons, 2010; Busch *et al.*, 2015). How stresses are distributed along such shapes is not yet fully understood. In this article, we discuss how theory can help us evaluate membrane stresses based on the observed shape.

Shape as a reporter of force
Many biomechanics textbooks present the postulate that the relationship between the applied load and the resulting deformation

FIGURE 1: Curvature generation in biological membranes (adapted from Chabanon *et al.*, 2017). Membrane curvature is controlled by different physical inputs including (A) protein-induced spontaneous curvature and (B) forces exerted by the cytoskeleton.

can be obtained if a constitutive relationship between the stress and strain of a material is given (Mofrad and Kamm, 2010; Phillips *et al.*, 2012; Fung, 2013). Indeed, the idea that shape can be considered a reporter of the applied force is an idea as old as continuum mechanics (Todhunter, 1886). A classical example illustrating how shape can be used as a reporter of force in biology can be understood by studying the shape of a vesicle or a cell using micropipette aspiration (Hochmuth, 2000; Lee and Liu, 2014). This method is used to calculate the tension of bilayer membranes in vesicles and cortical tension in cells through Laplace's law. Because the pressure applied by the micropipette is known, tension can be calculated using a force balance at the membrane.

Lee and coworkers suggested that membrane shape itself acts as a reporter of applied forces (Lee *et al.*, 2008) and calculated the axial force required to form membrane tethers in optical tweezer experiments based on shape, given the material properties of the membranes (see Figure 2 in Lee *et al.*, 2008). They showed that the calculated value of force was in excellent agreement with their experimental measurements. Separately, Baumgart and colleagues showed that the Gaussian modulus has a strong effect on membrane budding in phase-separated vesicles and that its magnitude

can be obtained by analyzing the geometry of the vesicle (Baumgart *et al.*, 2005).

An additional layer of complexity in how shape and forces are related arises through the heterogeneous composition of the lipid bilayer in cells. Most protein binding to cellular membranes represents a local process (Karotki *et al.*, 2011; Kishimoto *et al.*, 2011; Buser and Drubin, 2013). Even in in vitro studies, several groups have shown that protein adsorption on lipid domains can alter the lateral pressure profile on the bilayer and induce tubulation (Stachowiak *et al.*, 2012; Lipowsky, 2013; Zhao *et al.*, 2013). Recently, theoretical studies have shown that adsorbed proteins give rise to spontaneous surface tension (Lipowsky, 2013; Rangamani *et al.*, 2014b). Therefore, there is a need to understand how applied forces and membrane heterogeneity can regulate the local stresses on the membrane. Going beyond the approximation of tension using Laplace's law, we sought to understand the local stresses in tubes and buds—two geometries that are critical to many cellular phenomena. Using the well-established Helfrich model (Helfrich, 1973; Bassereau *et al.*, 2014) for membrane bending as a framework, we illustrate how local forces can be understood from the shape of the membrane. We close with an extended discussion of how advances in image analysis and measurement of material properties can aid in our understanding of how traction can be calculated from the curvature of the membrane.

LOCAL STRESSES IN THE MEMBRANE: GOVERNING EQUATIONS

Surface stress tensor and traction calculation

A general force balance for a surface ω, bounded by a curve ∂ω, is (Figure 2)

$$\int_\omega pn\,da + \int_{\partial\omega} \tilde{f}\,dt + F = 0 \tag{1}$$

where $t = r(s)\theta$ is the length along the curve of revolution perimeter (see Figure 2), p is the pressure difference across the membrane, $\tilde{f}$ is the traction along the curve of revolution t, and F is any externally applied force on the membrane. Along any circumferential curve on the membrane at constant z, the traction is given by (Agrawal and Steigmann, 2009a)

$$\tilde{f} = \tilde{f}_\nu \nu + \tilde{f}_n n + \tilde{f}_\tau \tau \tag{2}$$

The values of $\tilde{f}_\nu$, $\tilde{f}_n$, and $\tilde{f}_\tau$ will depend on the particular form of strain energy we choose to depict the membrane properties (see Figure 2 for definitions of the forces and the vectors). We choose the Helfrich Hamiltonian as the constitutive relationship in this case and use a modified version that includes spatially varying spontaneous curvature $C(\theta^\alpha)$, (Steigmann, 1999; Agrawal and Steigmann, 2009a; Hassinger *et al.*, 2017),

$$W = \kappa\left[H - C\left(\theta^\alpha\right)\right]^2 + \kappa_G K \tag{3}$$

where W is the energy per unit area, κ is the bending modulus, H is the local mean curvature, κ_G is the Gaussian modulus, K is the local Gaussian curvature, and θ^α denotes the surface coordinates. This form of the energy density accommodates the local heterogeneity in the spontaneous curvature C. Note

FIGURE 2: Schematic representing the axisymmetric coordinate system used for calculating curvature and traction. ω is the membrane surface area bounded by a curve $\partial\omega$, **f** is an externally applied force per unit area on the membrane, **n** is the normal vector to the surface, **ν** is the tangent to the surface in the direction of increasing arc length, e_r and e_z are unit vectors in radial and axial directions, τ is a unit vector tangent to the boundary in the direction of the surface of revolution, ψ is an angle made by the tangent with respect to the horizontal, θ is the angle of revolution, s is the arc-length parameterization, p is the transmembrane pressure difference, $\tilde{f}_r$ and $\tilde{f}_z$ are radial and axial tractions along the curve of revolution, respectively. Inset shows that pressure opposes traction and external force in both the radial and axial directions.

that W differs from the standard Helfrich energy by a factor of 2, which is accounted for by taking the value of κ to be twice that of the standard bending modulus typically encountered in the literature (see Supplemental Tables S1 and S2 for notation). A more in-depth investigation of the role of anisotropic spontaneous curvature using a version of the Helfrich energy that includes deviatoric curvature can be found in the Supplemental Material (Supplemental Eq. S11; Iglič et al., 2006; Lokar et al., 2012).

While Eqs. 1 and 3 are general expressions that are independent of coordinates, for illustrative purposes and ease of analysis, we will restrict further analysis to rotationally symmetric membrane deformations (Figure 2). Using principles of force balance, one can derive the "shape" equation and the tangential balance equation for the Helfrich energy (see Supplemental Material for detailed derivations). The traction, which is the force per unit length, across any boundary of constant z is given by

$$\underbrace{\tilde{f}_n}_{\substack{\text{Normal} \\ \text{traction}}} = -\kappa \underbrace{(H' - C')}_{\substack{\text{Curvature} \\ \text{gradient}}} \tag{4a}$$

$$\underbrace{\tilde{f}_v}_{\text{Tangential traction}} = \underbrace{\kappa (H - C)(H - C - \Psi')}_{\text{Curvature}} + \underbrace{\lambda}_{\text{Tension}} \tag{4b}$$

where ψ is the angle the membrane makes with the horizontal (see Figure 2), λ is the local membrane tension, and $()'$ denotes a derivative with respect to arc-length s, for example, $H' = dH/ds$.

From the above equations, we see that the normal traction, $\tilde{f}_n$, captures the effect of curvature gradients, while the tangential traction, $\tilde{f}_v$, captures the effect of local membrane tension and curvature. A complete derivation of the stress balance and the governing equations of motion is presented in the Supplemental Material. Additional derivations of traction, including spatially heterogeneous spontaneous bending and Gaussian moduli, anisotropic spontaneous curvature, and asymptotic approximations for small radius, are presented in the Supplemental Material.

Interpretation of traction

Traction, which has units of force per unit length, was initially introduced by physicists as a result of Noether's theorem (Capovilla and Guven, 2002a, 2004; Guven, 2004). This theorem states that, for any elastic surface that is in equilibrium, there exists a unique traction distribution such that its divergence is conserved (Guven, 2004). Mechanically, the traction distribution gives us information about the response of the membrane to externally applied loading, including forces acting on the membrane or protein-mediated bending. Many studies have derived these equations mathematically and sought to explain them in a biophysical context. Capovilla and Guven (Capovilla and Guven, 2002a,b, 2004) invoked the action-reaction law—if one were to cut the membrane along any curve, $\tilde{f}_n$ and $\tilde{f}_v$ are the forces per unit length of the curve in the normal and tangential directions, respectively, that the membrane on one side of the cut exerts on the other. Furthermore, the expressions for tractions (Eqs. 4) reduce to their corresponding fluid analogues for negligible membrane rigidity and pressure difference. Thus, we can interpret the normal and tangential tractions as follows: the tangential traction distribution tracks the gradient in "effective" surface tension (discussed in different examples below), while the normal traction distribution contains information regarding a force balance performed normal to the membrane at every point. Further physical interpretations of these quantities can be obtained based on the particular biological phenomena, as

illustrated below by examining two fundamental membrane deformations—tubes and buds.

Axial force and effective line tension

We obtain the formulae for traction in the axial and radial directions obtained by projecting the normal and tangential tractions onto these axes (Supplemental Eq. S28; full derivation is given in the Supplemental Material). We can then calculate the magnitude of an applied axial force on the membrane by integrating the axial component of the traction (Supplemental Eq. S28b) along the circumference of the bounding curve $\partial\omega$, yielding

$$\tilde{F}_z = 2\pi r \left[\underbrace{\kappa (H' - C')\cos(\Psi) + \kappa(H - C)(H - C - \Psi')\sin(\Psi)}_{\text{Bending contribution}} + \underbrace{\lambda \sin(\Psi)}_{\text{Tension contribution}} \right] \tag{5}$$

where $\tilde{F}_z$ is the axial force generated in response to an external load.

An energy per unit length, ξ, associated with deformations in the radial direction, can be found by integrating the radial traction along the curve $\partial\omega$ (Figure 2), as

$$\xi = 2\pi r \left[\underbrace{\kappa (H - C)(H - C - \psi')\cos(\psi)}_{\text{Curvature contribution}} + \underbrace{\lambda \cos(\psi)}_{\text{Tension contribution}} + \underbrace{\kappa(H' - C')\sin(\psi)}_{\text{Curvature gradient contribution}} \right] \tag{6}$$

ξ can be interpreted as an "effective" line tension (Seifert, 1997). While line tension denotes the force acting at the boundary of two interfaces—for example, inward force for a liquid droplet on a hydrophobic substrate and an outward force on a hydrophilic substrate (Buehrle et al., 2002; Liu et al., 2006)—the "effective" line tension predicts a general resistive force acting at every point opposing any change in the membrane length, regardless of a phase boundary. This "force" is not an actual radial force but represents the change in energy with respect to the characteristic length scale (McDargh et al., 2016); going forward, we refer to it as an energy per unit length.

Illustrative examples of traction along the membrane

For spherical vesicles, where the mean curvature is constant, and in the absence of spontaneous curvature ($C = 0$) and homogeneous composition, the normal traction $\tilde{f}_n$ is zero, because curvature gradients are zero (Eq. 4a), and the tangential traction, $\tilde{f}_v$, reduces to the membrane tension λ (Eq. 4b). This is consistent with previous discussions of membrane tension (Rangamani et al., 2014b). For surfaces with zero mean curvature (minimal surfaces such as catenoids; Powers et al., 2002) and homogeneous composition, $\tilde{f}_n$ is zero and $\tilde{f}_v$ is equal to λ, which is also consistent with the interpretation of membrane tension for these surfaces (Powers et al., 2002; Chabanon and Rangamani, 2018).

What happens when the mean curvature is not constant or the membrane is not homogeneous in composition? Given a membrane shape and a constitutive relationship, Eqs. 4a and 4b tell us that we can calculate the local stresses along the membrane. One way of studying shapes is to use images from high-resolution microscopy of membrane vesicles of known composition. However, these images can be noisy, and obtaining the local curvature and curvature gradients requires fitting the curve with multiple splines or other functions (Lee et al., 2008). Another way to generate
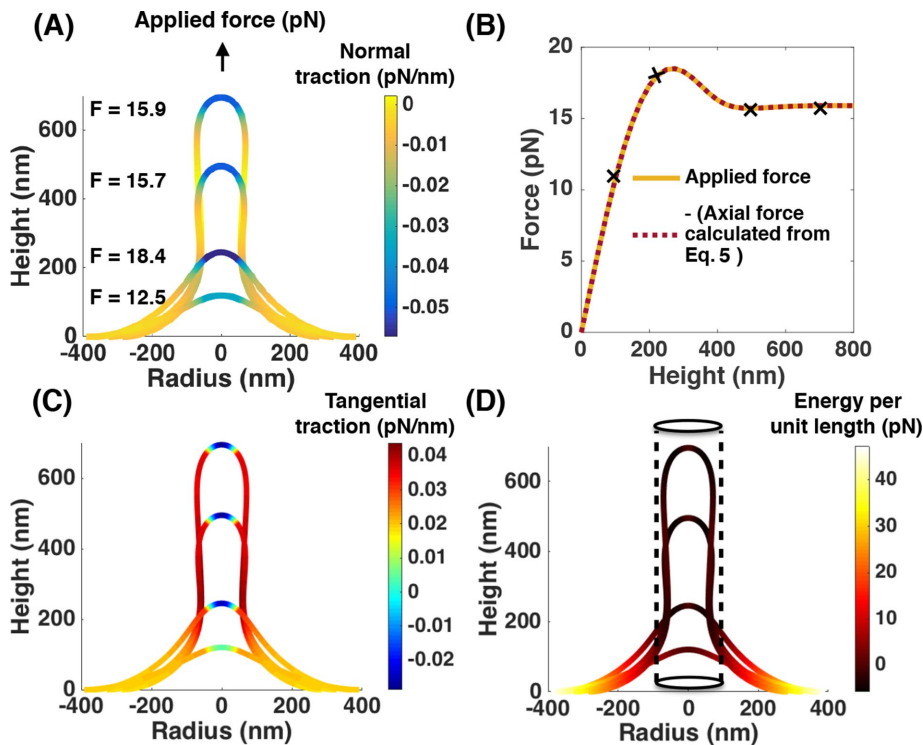
FIGURE 3: Analysis of normal and tangential traction for membrane tethers. (A) Normal traction distribution along four membrane tether shapes obtained by applying a point load of the specified magnitude at the pole, $\lambda_0 = 0.02$ pN/nm, $\kappa = 320$ pN·nm. (B) Magnitude of axial force as a function of tether height, showing an exact match between the force (Eq. 5) calculated from the traction distribution and obtained directly from the simulation. (C) Tangential traction distribution along the membrane shapes shown in A. (D) Energy per unit length calculated using Eq. 6 along the four membrane shapes shown in A. The dashed lines outline the equilibrium geometry for a membrane cylinder $R_0 = \frac{1}{2}\sqrt{\kappa/\lambda}$.

membrane shapes is to use simulations. Because our goal is to illustrate the concept of local tractions, we use shapes generated from simulations to elucidate how the normal and tangential tractions are distributed along the membrane. The traction distributions are not the direct output of these simulations; instead, they are calculated a posteriori using the output shapes from the simulations and the membrane properties, similarly to how one would calculate these distributions from experimentally observed membrane shapes.

## Tether formation due to applied load—revisiting a classical membrane deformation

The formation of membrane tethers in response to a point load is a classic example of force-mediated membrane deformation (Roux et al., 2002; Smith et al., 2004) that has been extensively studied both experimentally (Waugh, 1982; Heinrich et al., 1999) and theoretically (Derényi et al., 2002; Powers et al., 2002; Prévost et al., 2017; Simunovic et al., 2017). This comes as no surprise, because a tether is a starting point for understanding membrane deformation in a wide variety of biological contexts, including endocytosis, filopodial formation, and tubulation in the endoplasmic reticulum (ER). We used this example to validate our method and to identify how normal and tangential tractions contribute to the formation of tethers. We generated a membrane tether by applying a localized force at the pole to mimic a point load and solved the shape equation for homogeneous bilayers in axisymmetric coordinates (Supplemental Eq. S17) for a membrane tension of 0.02 pN/nm

(simulation details provided in the Supplemental Material).

The normal and tangential traction distributions along the tether are shown in Figure 3. The absolute value of the normal traction is highest at the pole as the applied force increases. The membrane curves away from the applied force along the region over which it is applied and conforms to a stable cylindrical geometry along the rest of the tether and a flat region at the base. The tangential traction has a large positive value along the cylindrical portion of the tether (Figure 3C), showing that the membrane resists stretching as the tube is pulled out. The tether cap has a negative tangential traction because of the membrane tension heterogeneity (Supplemental Eq. S10) induced by the application of the load. The corresponding radial and axial traction components (Supplemental Eqs. S28a and S28b) plotted along the equilibrium shapes are shown in Supplemental Figure S1.

As expected, the negative of the axial force (Eq. 5), evaluated at the base of the geometry, exactly matches the force-extension relationship for tether formation obtained directly from the simulation (see Figure 3B), showing that the local stresses along a membrane shape can help us evaluate the applied forces. We also considered the role of a large turgor pressure that opposes the membrane invagination, mimicking the situation in yeast endocytosis (Basu et al., 2014; Aghamohammadzadeh and Ayscough, 2009; Dmitrieff and Nédélec, 2015). Transmembrane pressure results in an additional term in the axial traction (see Supplemental Eq. S29). As seen in Supplemental Figures S2 and S3, an excellent match between the applied load and the calculated force from the traction distribution is obtained for simulations with pressure by modifying our expression for force. We further verified that our results are independent of the system constraints (i.e., conserved arc length or surface area), confirming that changes in membrane area do not change the validity of our approach (Supplemental Figure S7).

What information do the tangential tractions contain? The tangential tractions play an important role in squeezing the membrane neck and holding the cylindrical configuration during membrane elongation (see Supplemental Figure S1). Consequently, in Figure 3D, the point of zero "effective" line tension corresponds to the dotted cylinder, which has a radius of $R_0 = \frac{1}{2}\sqrt{\kappa/\lambda}$ (Derényi et al., 2002). This equilibrium cylinder has no curvature gradient, leading to zero "effective" line tension. The calculated values of energy per unit length inside the cylinder are negative, while those outside are positive, suggesting that the "effective" line tension indicates the extent of deviation from the idealized cylindrical geometry. A negative energy per unit length here refers to the fact that there exists a negative radial force at the point (McDargh et al., 2016). Additionally, the value of ξ at the neck is ~3 pN, providing an estimate of the effective line tension required to form a neck in tethers.
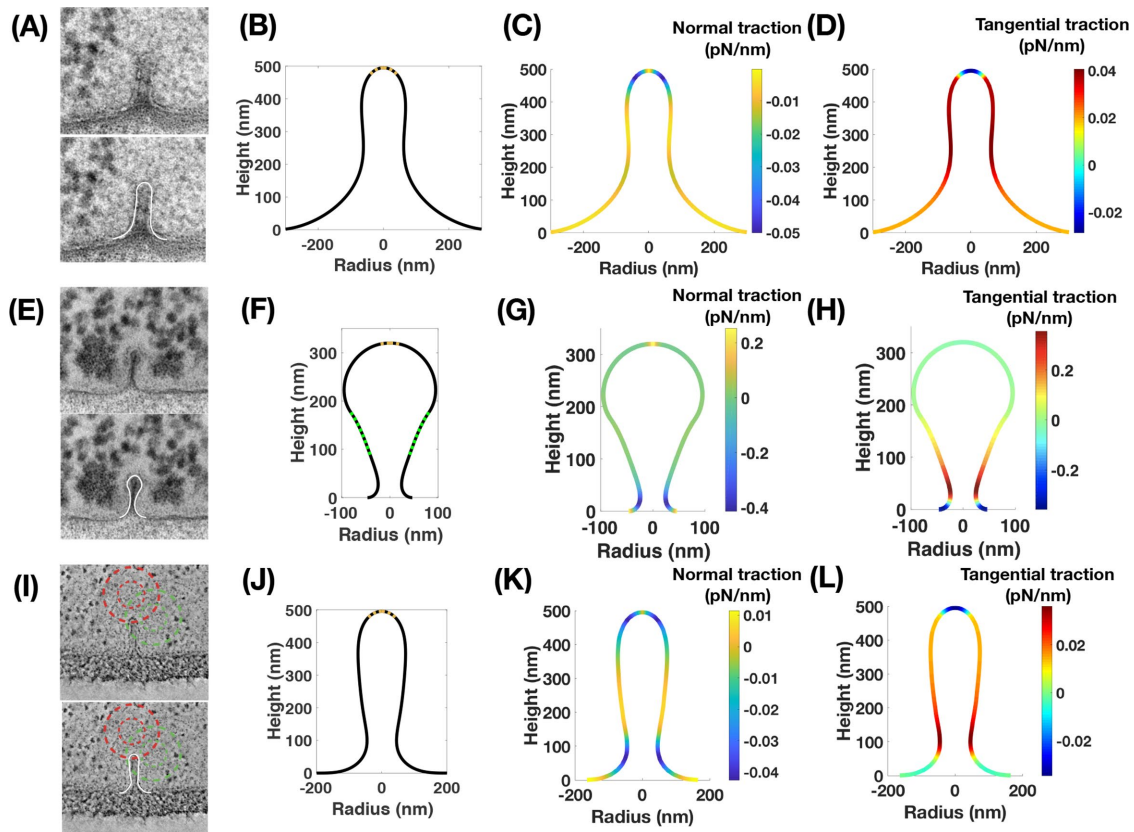
FIGURE 4: Comparison of normal and tangential tractions between multiple mechanisms of membrane tether formation. (A) EM image of an endocytic PM invagination in a bzz1Δrvs167Δ yeast cell (Kishimoto *et al.*, 2011). Top, original EM image; bottom, EM image with traced membrane shape (white). (B) Simulated membrane shape obtained by application of a point force (brown), $\lambda_0 = 0.02$ pN/nm, $\kappa = 320$ pN·nm. (C) Normal traction distribution along the membrane shape in B. (D) Tangential traction distribution along the membrane shape in B. (E) EM image of an endocytic PM invagination in a wild-type yeast cell (Kishimoto *et al.*, 2011). Top, original EM image; bottom, EM image with traced membrane shape (white). (F) Simulated membrane shape obtained by application of an anisotropic spontaneous curvature (green) along the tubular section of a membrane tether, $\lambda_0 = 0.02$ pN/nm, $\kappa = 320$ pN·nm, $C = -0.01$ nm^{-1}, $D = 0.01$ nm^{-1}. (G) Normal traction distribution along the membrane shape in F. (H) Tangential traction distribution along the membrane shape in F. (I) Electron tomography image of an endocytic invagination in budding yeast (Kukulski *et al.*, 2012). Top, original EM image; bottom, EM image with traced membrane shape (white). (J) Simulated membrane shape obtained by application of a point force (brown) against an equivalent pressure to the membrane tension in B, $\lambda_0 = 0.02$ pN/nm, $\kappa = 320$ pN·nm, $p = 0.3$ kPa. (K) Normal traction distribution along the membrane shape in J. (L) Tangential traction distribution along the membrane shape in J.

Traction along tubes is highly dependent on mechanisms of membrane deformation and resistive force

Do all membrane tubes have the same traction distribution? To answer this question, we compared membrane shapes that look superficially similar and calculated the traction profiles along them (Figure 4). We show that different tubes can have very different tractions depending on the mechanism of membrane deformation and the resistive forces that are acting on them. We begin by comparing electron micrographs of yeast endocytic invaginations in mutant cells lacking the BAR domain proteins Bzz1 and Rvs167 and wild-type cells (Kishimoto *et al.*, 2011) (Figure 4, A and E, respectively). Because force from actin assembly is the primary driver of membrane deformation in this process (Kukulski *et al.*, 2012), we assume that the deformation in the mutant cell is a result of having only an applied force at the tip of the invagination (Figure 4B). In the wild-type case, we assume that the BAR domain proteins induce an anisotropic spontaneous curvature locally (e.g., tubulation) (Frost *et al.*, 2009) (Figure 4F; see Supplemental Figure S10 and

Supplemental Material for implementation and traction calculation). These assumptions between the mutant and wild-type cells are simplifications, but serve to illustrate the differences in traction distribution. In particular, the tangential traction in the wild-type case (Figure 4H) is nearly zero near the tip of the bud and highest near the base, in stark contrast to the mutant, which lacks additional curvature generation and therefore is high all along the tube (Figure 4D). These results suggest that the BAR domain proteins can act as a barrier to the stresses induced by the axial force, which is consistent with recent experimental evidence that points to a potential scission mechanism (Simunovic *et al.*, 2017). Indeed, a negative normal traction at the tube base in Figure 4G demonstrates a tendency for the neck to shrink in size.

The previous simulations were conducted using a membrane tension that is applicable to mammalian cells (Sens and Plastino, 2015). However, turgor pressure is thought to be the primary opposing force in yeast endocytosis (Aghamohammadzadeh and Ayscough, 2009). To investigate the role of turgor pressure, we performed a
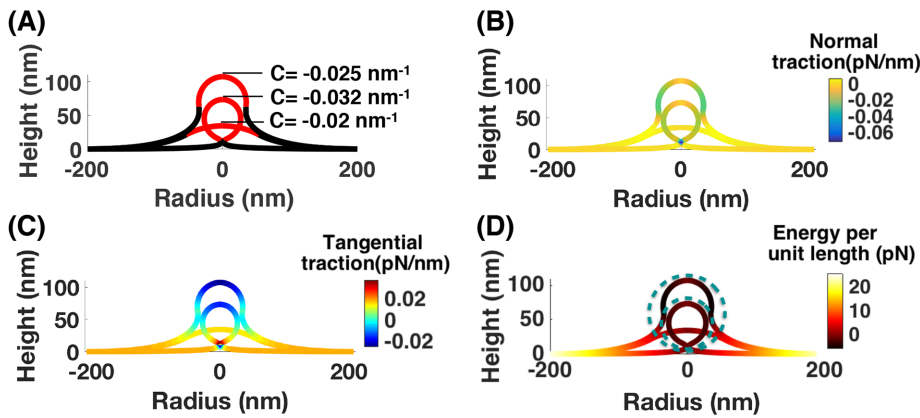
FIGURE 5: Analysis of budding due to protein-induced spontaneous curvature and calculation of line tension. Simulations were conducted with (A = 10,053 nm²) spontaneous curvature at the center of an initially flat patch increasing from $C = 0$ to $C = 0.032$ nm⁻¹, $\lambda_0 = 0.02$ pN/nm, κ = 320 pN·nm, $p = 0$ (Hassinger et al., 2017). (A) Membrane shapes for three different spontaneous curvature distributions, with the value of C indicated in the red region and zero in the black region. (B) Normal traction along the membrane for the shapes shown in A. (C) Tangential traction distribution along the shapes shown in A. (D) Energy per unit length distribution for the three different shapes. The dashed line circles outline spheres with mean curvatures H = 0.032 nm⁻¹ (smaller circle) and H = 0.025 nm⁻¹ (larger circle).

simulation in which the value of the turgor pressure was set such that the radius of the resulting tube (Figure 4J) would match that of the tube generated using membrane tension (Figure 4B). The normal traction distribution in this case (Figure 4K) is strikingly different; there is a large negative normal traction at the base of the tube, indicating that turgor pressure acts to induce the formation of a neck. The tangential traction (Figure 4L) is no longer uniform on the tube and is again greatest just above the narrowing of the tube at the base. Though these simulations are only meant to capture the approximate shapes of the membrane in these different cases and do not necessarily match the length scales or parameter values with respect to the biological situations, they serve to illustrate the point that the quantitative differences in the deformations against membrane tension and turgor pressure can be realized by calculating the local tractions along the membrane shape.

Formation of buds due to spontaneous curvature is characterized by an emergent line tension

Phase separation and lipid domains are classical mechanisms of bud formation and vesiculation (Richmond et al., 2011). Previously, we and others have shown that protein-induced heterogeneity on the membrane can be modeled using a spontaneous curvature field (Steigmann, 1999; Agrawal and Steigmann, 2009b; Rangamani et al., 2014b). We used this framework to investigate the nature of membrane tractions generated during budding due to a spontaneous curvature field. We conducted simulations for a constant area of the spontaneous curvature field $A = 10,000$ nm² and varied the extent of spontaneous curvature, C, from 0 to 0.032 nm⁻¹ (Figure 5A). We calculated the value of traction for three distinct shapes: a shallow invagination, a U-shaped bud, and a closed Ω-shaped bud (Figure 5, B–D).

The normal traction is negative along the applied spontaneous curvature field, indicating a sharper change in mean curvature compared with the applied spontaneous curvature ($H' > C'$ in Eq. 4a). At the neck, where $\psi = \pi/2$, normal traction is maximum and acts purely inward, representing the tendency of the membrane to form small necks. The tangential traction shows a change in sign from

positive to negative as the neck radius becomes smaller. This change in sign highlights the critical role of the gradient in tangential traction in the formation of narrow necks (Hassinger et al., 2017) (Figure 5, B–D). The dashed circles represent the equilibrium spherical vesicles calculated by Helfrich energy minimization ($R_{vesicle} = \dfrac{\kappa C}{\lambda + \kappa C^2}$) (Hassinger et al., 2017). The positive tangential traction in tent-like small deformations indicates that the membrane resists the bending deformation; however, in the U-shaped and closed buds, the negative tangential traction along the cap acts to pull the membrane inward and favors the adoption of a highly curved shape. The radial and axial tractions distribution along all three shapes are shown in Supplemental Figure S4, which reveals that bud formation by spontaneous curvature is purely driven by radial traction, while axial traction is zero everywhere.

Each equilibrium bud divides the membrane into two domains: 1) the membrane inside the bud with negative energy per unit length that bends to form a bud and 2) the membrane outside the bud with positive energy per unit length that resists such a deformation. Previously, both modeling and experimental studies have shown that, in heterogeneous membranes, line tension can be sufficient for scission of endocytic pits (Liu et al., 2006) or the formation of buds in vesicle experiments (Baumgart et al., 2003, 2005). In the case of an applied spontaneous curvature field, the expression of energy per unit length (Supplemental Eq. S31) can be interpreted as the actual line tension at the interface of the two phases. Through the process of bud formation, line tension undergoes a sign change from positive (acting outward) to negative (acting inward), effectively transitioning from a tension-dominated regime to a curvature gradient–dominated regime (Figure 6). This transition from positive to negative line tension with increasing value of spontaneous curvature is also observed in other studies (Dan and Safran, 1998). The value of the energy per unit length at the interface varies between –5 and 5 pN, which is in the same order of magnitude as reported interfacial line tension between coexisting phases in lipid bilayers (Lipowsky, 1992; Liu et al., 2006).

There are two other factors that could affect the traction distribution along the bud: 1) a change in area of the membrane during budding and 2) spatial heterogeneity in membrane moduli. To explore how the change of membrane area influences bud formation mediated by protein-induced spontaneous curvature, we conducted a simulation with a fixed available arc length instead of area (Supplemental Figure S6). Similar to the case of a homogeneous membrane with fixed area, the energy per unit length at the interface changes sign from positive to negative in a range of –5 to 5 pN. However, protein segregation on the membrane can lead to heterogeneity in material properties such as bending moduli (Jin et al., 2006). To investigate the effect of this spatial heterogeneity in the bending moduli along the membrane surface, we repeated the budding simulation from Figure 5, assuming that the bending rigidity along the spontaneous curvature field is 7.5 times larger than the bending rigidity of the bare membrane (Supplemental Figure S5) (Jin et al., 2006). Because the membrane is stiffer and
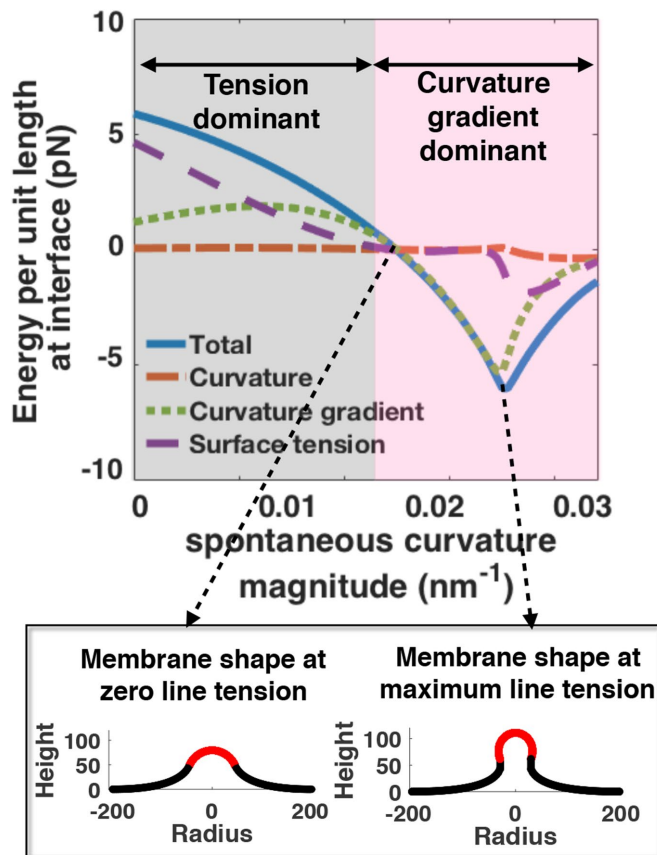
FIGURE 6: Change in energy per unit length and its components at the interface with increasing spontaneous curvature. Two regimes are observed: a surface tension–dominated regime for small value of spontaneous curvature and a curvature gradient–dominated regime for large values of spontaneous curvature. The membrane configurations are shown for two spontaneous curvatures: $C = -0.02$ nm^{-1}, where energy per unit length at interface is zero; and $C = -0.025$ nm^{-1}, where energy per unit length is maximum. The red domains show the region of spontaneous curvature for the corresponding shapes.

harder to bend, a wider neck is formed at $C = -0.032$ nm^{-1} compared with the case of a uniform membrane (Supplemental Figure S5A) (Hassinger et al., 2017). This membrane resistance to deformation is observed as a uniform positive normal traction everywhere along the membrane (Supplemental Figure S5A). To compare the behavior of the line tension at the edge of the spontaneous curvature field, we ran the budding simulation with the spatially heterogeneous bending moduli up to a larger value of spontaneous curvature ($C = -0.035$ nm^{-1}) in order to have the same range of neck radii as the uniform membrane (Figure 5E). We can see that the trend of line tension variation versus the spontaneous curvature is almost the same in both cases (Supplemental Figure S5E), changing sign from positive to negative followed by a critical point indicating the transition from a U- to an Ω-shaped bud. However, the magnitude of line tension is different in the two cases. For small magnitudes of spontaneous curvature (tent-shaped buds), the average difference in line tension is ~1 pN. But for large magnitudes of spontaneous curvature ($C \geq -0.0275$ nm^{-1}, Ω-shaped buds), the average line tension for a rigid coat is ~4 pN larger than the line tension in a homogeneous membrane. This larger value of line tension in a heterogeneous membrane has been reported in various

experimental measurements (Lipowsky, 1992; Tian et al., 2007) and other theoretical studies (Kuzmin et al., 2005; Semrau and Schmidt, 2009).

Traction distribution is a signature of distinct budding mechanisms

Conceptually, there are two primary means by which membrane buds can be maintained: an accumulation of protein- or lipid-induced spontaneous curvature favoring a spherical geometry, or a constriction force that pinches the membrane into a budded shape. In Figure 7, we illustrate the traction distribution in these two cases. The upper row represents spontaneous curvature-induced budding, meant to resemble vesicle coat protein (such as the coatomer COPII)-mediated budding from the ER (Robinson et al., 2015; Figure 7A), and the lower row represents budding due to a local constriction force via a contractile ring in budding yeast (Mozdy et al., 2000; Figure 7E). Although the two simulated shapes are superficially similar, the traction distributions are quite different. The normal traction distribution for spontaneous curvature budding (Figure 7C) is similar to the one seen in Figure 5, where there is a large negative traction at the bud neck, indicating forces acting to minimize the neck radius. Conversely, for the constriction force budding, the normal traction is highly positive at the neck (Figure 7G), indicating a resistance by the membrane to the applied force. The tangential tractions (Figure 7, D and H) are also quite different. For example, moving from the top to the bottom of the vesicle, the tangential traction in the case of the protein-induced spontaneous curvature budding is initially negative and then positive after the neck (Figure 7D). However, for the constriction force–mediated budding, the tangential traction is positive at first and then negative after the neck (Figure 7D).

This difference in the gradient of tangential traction at the membrane neck serves as a signature for spontaneous curvature-mediated versus force-mediated bud formation. Thus, the mechanism of curvature generation can be related to the computed traction profile, and some a priori knowledge can help uncover these differences (see Figures 4 and 7).

Another mechanism of maintaining membrane buds (specific to endocytosis) is through actin-mediated forces, wherein an actin network polymerizes in a ring at the base of the plasma membrane (PM) invagination and is connected to the coat, driving inward movement (Picco et al., 2015; Walani et al., 2015). We have previously considered these cytoskeletal effects in Hassinger et al. (2017) and show here that the applied forces can be matched to axial forces calculated from traction (Supplemental Figures S8 and S9) for two orientations of the applied force.

Sensitivity analysis and sources of errors

In principle, calculating force from shape is at the heart of stress–strain relationships. However, there are some fundamental challenges associated with sources of errors in such a calculation. There are two main sources of errors: error in the measurement of material properties (membrane bending modulus and membrane tension) and error in the measurement of shape. We present some simple analysis of these sources of error in what follows.

Parametric sensitivity analysis of material properties. Ideally, one would like to define a sensitivity index similar to the parametric sensitivity conducted for systems of chemical reactions, where the sensitivity of a quantity F_i with respect to a parameter κ_i is given by $S_{i,j} = \partial F_i / \partial \kappa_j$ (Varma et al., 2005). However, because we wish to simultaneously explore the effect of both the bending modulus and
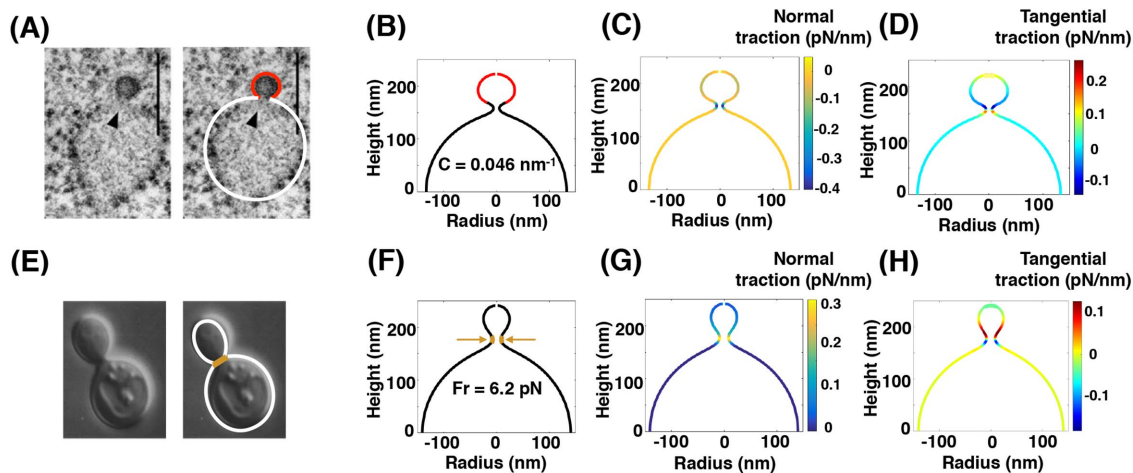
FIGURE 7: Comparison of normal and tangential tractions between two different mechanisms of membrane budding. (A) EM image of COPII budding from the ER in green algae (Robinson *et al.*, 2015). Left, original EM image; right, EM image with traced membrane shape. Red, COPII coat; white, bare membrane. (B) Simulation of bud formation on a hemispherical cap using a constant spontaneous curvature (*C* = −0.046 nm⁻¹, red). (C) Normal traction distribution along the membrane shape in B. A large negative normal traction can be seen at the neck of the formed vesicle. (D) Tangential traction distribution along the membrane shape in B. There is a change in the sign of the tangential traction before and after the bud neck. (E) Bright-field microscopy image of a budding yeast (Mozdy *et al.*, 2000). Left, original EM image; right, EM image with traced membrane shape. Brown, contractile ring at the bud neck. (F) Simulation of bud formation on a hemispherical cap with a constant radial force (*F*ᵣ = 6.2 pN, yellow) that locally constricts the hemisphere to form a bud. (G) Normal traction distribution along the membrane shape in F. There is a positive normal traction at the vesicle neck in response to the applied force. (H) Tangential traction distribution along the membrane shape in F.

tension, we use a simple linear calculation of error. Uncertainties in either of these quantities will result in an uncertainty in the traction and the calculated axial force and energy per unit length (Eqs. 5 and 6). Here, we assume that the bending modulus and membrane tension can be written as $\kappa = \kappa_{mean} \pm \kappa_{error}$ and $\lambda = \lambda_{mean} \pm \lambda_{error}$, respectively. Then, by virtue of the relationships in Eqs. 5 and 6, we can estimate the error in the axial force and the energy per unit length as

$$F_{z,error} = \pm 2\pi r \left[\begin{array}{c} \kappa_{error}(H' - C')\cos(\psi) \\ + \kappa_{error}(H - C)(H - C - \psi')\sin(\psi) + \lambda_{error}\sin(\psi) \end{array} \right] \quad (7a)$$

$$\xi_{error} = \pm 2\pi r \left[\begin{array}{c} \kappa_{error}(H - C)(H - C - \psi')\cos(\psi) \\ + \kappa_{error}(H' - C')\sin(\psi) + \lambda_{error}\cos(\psi) \end{array} \right] \quad (7b)$$

These equations allow us to interrogate how errors in both membrane moduli and membrane tension affect the error in forces. We took our control to be the output of tubulation and budding simulations described in Figures 3 and 5, respectively. Then, we conducted the same simulations over a range of bending moduli and membrane tensions to reflect a range in error of these two quantities. From these simulations, we 1) calculated the applied force, using Eq. 5 for the tube-pulling simulations at the peak of the force-displacement plot; and 2) the energy per unit length at the phase boundary, using Eq. 6 for the budding simulations at the same value of spontaneous curvature. Figure 8, A and C, shows the result of this procedure for a force and energy per unit length respectively that have been normalized to the output from the initial simulations (as indicated by "x"). As expected, separately varying either bending modulus or membrane tension is translated into an error in the force and energy per unit length, though the

magnitude of the final error does not match that of the input error due to the coupling to shape (Eqs. 5 and 6). Next, we investigate the nonlinear effect on the computed errors of varying bending modulus and membrane tension simultaneously. Interestingly, we see that, in some cases, the error in one parameter is compensated for by the error in the other, as highlighted by the dashed lines, which indicate a band of less than 10% total error. This is due to the intrinsic scaling in both tubulation (Derényi *et al.*, 2002; Dmitrieff and Nédélec, 2015) and budding (Hassinger *et al.*, 2017) with respect to bending modulus and membrane tension. Overall, we observe that the final error is not simply a sum of the errors in the two material properties, and compensatory behaviors can result (Eqs. 7; Figure 8, A and C).

In the previous calculation, when the membrane modulus and tension were varied, both the characteristic length of the membrane and its shape were affected. We conducted another analysis, in which the shape of the membrane was fixed to the control and an error was introduced in the values of bending modulus and membrane tension during the calculation of tractions (Figure 8, B and D). Interestingly, we found that the error in the axial force is independent of the error in membrane tension (Figure 8B). This is a consequence of calculating the axial force at a point at the base of the deformation, where the angle ψ is almost zero, and so, the tension term contributes less. If one were to instead perform the force balance at a point on the membrane where ψ is not zero, the error in the force would again depend on the error in both bending modulus and tension (Supplemental Figure S11). This, in principle, could be beneficial, in the sense that one could minimize the error in determining the axial force by evaluating it at a location where the total error is minimized (e.g., if uncertainty in membrane tension is large, calculate the applied force at the base of the invagination, because the calculation is insensitive to error in membrane tension at this location).
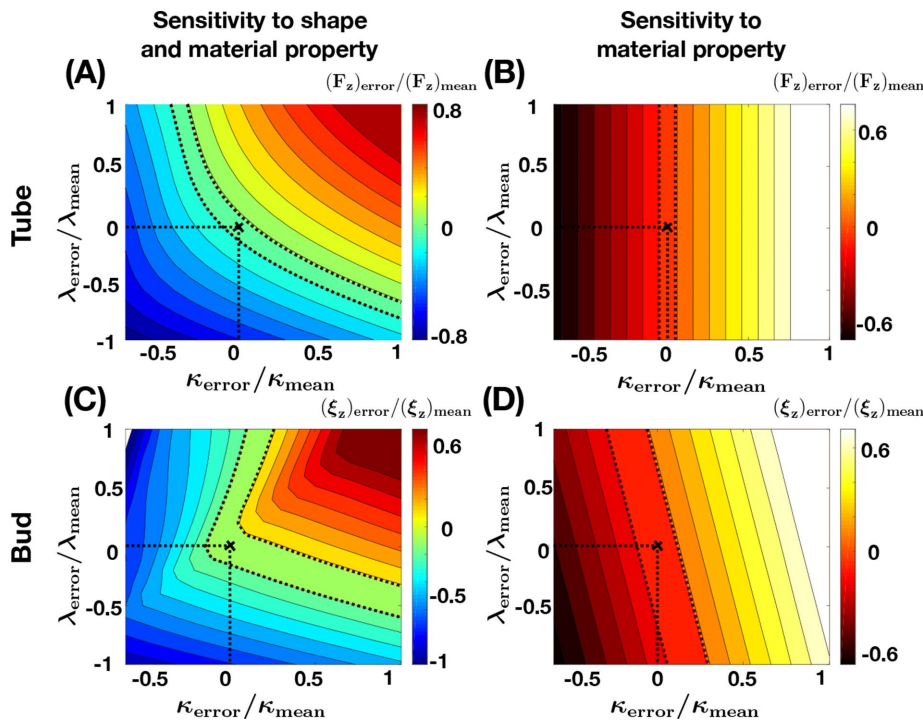
FIGURE 8: Parametric sensitivity analysis to material properties. Axial force (Eq. 5) and energy per unit length (Eq. 6) were calculated for a variation in the bending rigidity κ and membrane tension λ_0 both in membrane tubes (A, B) and buds (C, D). Dashed lines indicate 10% error. $\lambda_{mean} = 0.02$ pN/nm, $\kappa_{mean} = 320$ pN·nm, $-(F_z)_{mean} = 18$ pN (corresponding to a tube of height 300 nm in Figure 3), $\xi_{mean} = 6.13$ pN (corresponding to a spontaneous curvature of 0.0276 nm^{-1} in Figure 5). The sensitivity analysis was performed in two ways. 1) Sensitivity to shape and material property by running multiple simulations corresponding to the different parameter values (A, C), followed by an error calculation with respect to the mean value. 2) Sensitivity to only material property by using a range of parameter values during calculation of axial force (Eq. 5) and energy per unit length (Eq. 6) for a single simulation (mean) (B, D). (A) Sensitivity to shape and material property in a membrane tube. (B) Sensitivity to only material property in a membrane tube. (C) Sensitivity to shape and material property in a membrane bud. (D) Sensitivity to only material property in a membrane bud.

In contrast, the phase boundary is located at a particular position on the membrane curve and so must be evaluated at that point. We observe that the dependence of the error in the energy per unit length on bending modulus and membrane tension is no longer nonlinear (Figure 8D) as we fix the shape of the membrane and vary the material properties. Further, we see that the primary dependence of the error in the energy per unit length comes from the error in the bending modulus. Finally, we once again see that the total error is less than the sum of its two contributions due to the coupling to the local membrane shape, as expected from Eqs. 7.

Errors in quantification of shape metrics. One of the largest source of errors in calculating forces arises from imaging modalities for shape itself. Uncertainty in the shape of the membrane will depend on the method used to extract shapes from microscopy images. Additionally, the high curvatures at endocytic sites mean that a higher imaging resolution is required. Live-cell light microscopy is limited in resolution (even in superresolution methods; Wäldchen *et al.*, 2015; Sydor *et al.*, 2015), and traditional electron microscopy (EM) following chemical fixation may not fully preserve the shape of the bilayer (Bozzola and Russell, 1999; Stephens and Allan, 2003). To this end, cryoelectron tomography may provide the best preservation, but it suffers from anisotropic resolution as a result of the "missing wedge" effect (Lučić *et al.*, 2013). As a result, error can be

introduced into the fundamental position and geometric variables of the constitutive equations associated with the membrane deformation. Errors in the position and shape coordinates, coupled with nonaxisymmetric geometries, can result in nonlinear error propagation in the calculations, and their effects are not yet understood.

DISCUSSION

In this study, we presented a framework for the calculation of axial and radial tractions for nonlinear deformations of the membrane in the absence and presence of heterogeneities, solely based on the membrane geometry and material properties. From these calculations, we summarize that 1) tether formation requires both axial and radial tractions (Figure 3), and 2) line tension can be calculated between two phases as an energy per unit length (Figure 6). Importantly, using different examples of critical membrane shapes that occur in endocytosis and exocytosis, we have demonstrated that the local tractions are directly related to deviations from idealized geometries and can be generated by membrane heterogeneity. Moving forward, this procedure can be useful for the analysis of forces acting on membranes, both in reconstituted systems and in cells.

Using the analysis presented here and having some knowledge of the shape and material properties will allow us to estimate the local stresses acting on a membrane. It is important to note that the tractions calculated here depend on the knowledge of the membrane strain energy and the material properties.

It has been demonstrated that PEGylation of lipids (Lee and Pastor, 2011), amphiphilic block copolymers (Lim *et al.*, 2017), and protein crowding (Snead *et al.*, 2017) can curve and even induce scission of artificial lipid bilayers. In addition to material properties, nonlinear interactions between curvature-inducing proteins, membrane curvature, and protein aggregation play an important role in governing the molecular mechanisms by which proteins sense and induce curvature (Mesarec *et al.*, 2016). A theoretical treatment of the corresponding energy terms is in given in Gov (2018). Additional energy terms such as adhesion energy, entropic contributions from proteins, protein crowding, tilt, and cytoskeletal interactions will alter the expressions for tractions and introduce more material properties (Rangamani *et al.*, 2014a; Snead *et al.*, 2017; Carlsson, 2018). We also demonstrate that the knowledge of the underlying biophysical mechanism becomes important, because the shape of the membrane, particularly in cells, is a many-to-one function (multiple processes can give rise to a similar shape). However, the fundamental principle that shape contains information about the underlying forces will apply regardless of the exact form of the energy used to perform the analysis.

There can be multiple sources of error in the quantification of forces—error in the measurement of material properties, error in the measurement of the shape itself due to imaging, and finally, error in the assumptions about stress–strain relationships themselves. While

many of the measurements of material properties are conducted in vitro, recently, some studies have begun to measure the in vivo structure of lipids and their material properties (Nickels *et al.*, 2017). Interestingly, recent works also suggest that there is no long-range propagation of membrane tension in cells, seemingly reducing the uncertainty in calculating tension (Shi *et al.*, 2018). Additionally, efforts will need to focus on the development of image analysis methods to extract the shape of the membrane while reducing noise. There are already quite a few efforts in this direction, although these are focused on tension-based mechanisms in epithelial sheets. Curvature-dependent effects are harder to discern from imaging data (Brodland *et al.*, 2014; Veldhuis *et al.*, 2015). There is also a need for the development of algorithms that do not a priori assume symmetry of the shape and can handle irregular geometries. Then, imaging data, which are abundant in the literature (Frost *et al.*, 2009; Dannhauser and Ungewickell, 2012; Snead *et al.*, 2017), can potentially be analyzed and used to populate a database/machine-learning framework. This can then be extended to analyze the shapes of complex structures in cells, which likely include contributions from multiple mechanisms. Finally, an assumption that we have made in this study is to neglect the surrounding fluid flow or inertial dynamics and assume that the membrane is at mechanical equilibrium at all times (Naghdi, 1973; Steigmann *et al.*, 2003; Deserno, 2015). This assumption is commonly used in the modeling of membrane curvature to keep the mathematics tractable (Steigmann, 1999; Deserno, 2015). While the Helfrich model has been used by us and others with great success, the role of these dynamics of deformations, thermal fluctuations (Monzel and Sengupta, 2016; Steinkühler *et al.*, 2018), and multiscale models will be needed to truly appreciate different spatial and temporal scales of forces. In fact, thermal fluctuations coupled with protein aggregation can lead to runaway instabilities and scission (Shlomovitz *et al.*, 2011; Roux *et al.*, 2005) and must be considered in theoretical treatments. As a small step in this direction, we have implemented a modified form of the Helfrich energy including deviatoric effects to consider the anisotropic nature of spontaneous curvature (Supplemental Figure S10). While our current focus has been on explaining the mathematical and physical basis of local tractions and how these tractions can be used to understand important experimental systems and biological processes, to close the gap between modeling and experiments, future efforts will need to focus on relaxing the assumption of rotational symmetry and the ability to estimate local tractions in experimentally observed membrane shapes.

ACKNOWLEDGMENTS

REFERENCES

Aghamohammadzadeh S, Ayscough KR (2009). Differential requirements for actin during yeast and mammalian endocytosis. Nat Cell Biol 11, 1039.

Agrawal A, Steigmann DJ (2009a). Boundary-value problems in the theory of lipid membranes. Continuum Mech Thermodyn 21, 57–82.

Agrawal A, Steigmann DJ (2009b). Modeling protein-mediated morphology in biomembranes. Biomech Model Mechanobiol 8, 371–379.

Aimon S, Callan-Jones A, Berthaud A, Pinot M, Toombes GE, Bassereau P (2014). Membrane shape modulates transmembrane protein distribution. Dev Cell 28, 212–218.

Bassereau P, Sorre B, Lévy A (2014). Bending lipid membranes: experiments after W. Helfrich's model. Adv Colloid Interface Sci 208, 47–57.

Basu R, Munteanu EL, Chang F (2014). Role of turgor pressure in endocytosis in fission yeast. Mol Biol Cell 25, 679–687.

Baumgart T, Das S, Webb W, Jenkins J (2005). Membrane elasticity in giant vesicles with fluid phase coexistence. Biophys J 89, 1067–1080.

Baumgart T, Hess ST, Webb WW (2003). Imaging coexisting fluid domains in biomembrane models coupling curvature and line tension. Nature 425, 821–824.

Bozzola JJ, Russell LD (1999). Electron Microscopy: Principles and Techniques for Biologists, Sudbury, MA: Jones & Bartlett Learning.

Brodland GW, Veldhuis JH, Kim S, Perrone M, Mashburn D, Hutson MS (2014). CellFIT: a cellular force-inference toolkit using curvilinear cell boundaries. PLoS One 9, e99116.

Buehrle J, Herminghaus S, Mugele F (2002). Impact of line tension on the equilibrium shape of liquid droplets on patterned substrates. Langmuir 18, 9771–9777.

Busch DJ, Houser JR, Hayden CC, Sherman MB, Lafer EM, Stachowiak JC (2015). Intrinsically disordered proteins drive membrane curvature. Nat Commun 6, 7875.

Buser C, Drubin DG (2013). Ultrastructural imaging of endocytic sites in *Saccharomycescerevisiae* by transmission electron microscopy and immunolabeling. Microsc Microanal 19, 381–392.

Capovilla R, Guven J (2002a). Geometry of lipid vesicle adhesion. Phys Rev E 66, 041604.

Capovilla R, Guven J (2002b). Stresses in lipid membranes. J Phys A: Math Gen 35, 6233.

Capovilla R, Guven J (2004). Stress and geometry of lipid vesicles. J Phys Condens Matter 16, S2187.

Carlsson AE (2018). Membrane bending by actin polymerization. Curr Opin Cell Biol 50, 1–7.

Chabanon M, Rangamani P (2018). Gaussian curvature directs the distribution of spontaneous curvature on bilayer membrane necks. Soft Matter 14, 2281–2294.

Chabanon M, Stachowiak JC, Rangamani P (2017). Systems biology of cellular membranes: a convergence with biophysics. Wiley Interdiscip Rev Syst Biol Med 9.

Dan N, Safran S (1998). Effect of lipid characteristics on the structure of transmembrane proteins. Biophys J 75, 1410–1414.

Dannhauser PN, Ungewickell EJ (2012). Reconstitution of clathrin-coated bud and vesicle formation with minimal components. Nat Cell Biol 14, 634–639.

Derényi I, Jülicher F, Prost J (2002). Formation and interaction of membrane tubes. Phys Rev Lett 88, 238101.

Derganc J, Čopič A (2016). Membrane bending by protein crowding is affected by protein lateral confinement. Biochim Biophys Acta 1858, 1152–1159.

Deserno M (2015). Fluid lipid membranes: from differential geometry to curvature stresses. Chem Phys Lipids 185, 11–45.

Dmitrieff S, Nédélec F (2015). Membrane mechanics of endocytosis in cells with turgor. PLoS Comput Biol 11, e1004538.

Einstein D, Reinhall P, Nicosia M, Cochran R, Kunzelman K (2003). Dynamic finite element implementation of nonlinear, anisotropic hyperelastic biological membranes. Comput Methods Biomech Biomed Eng 6, 33–44.

Farsad K, De Camilli P (2003). Mechanisms of membrane deformation. Curr Opin Cell Biol 15, 372–381.

Ford MG, Mills IG, Peter BJ, Vallis Y, Praefcke GJ, Evans PR, McMahon HT (2002). Curvature of clathrin-coated pits driven by epsin. Nature 419, 361.

Fournier J-B (2007). On the stress and torque tensors in fluid membranes. Soft Matter 3, 883–888.

Frost A, Unger VM, De Camilli P (2009). The bar domain superfamily: membrane-molding macro-molecules. Cell 137, 191–196.

Fung Y-C (2013). Biomechanics: Mechanical Properties of Living Tissues, Heidelberg, Germany: Springer Science & Business Media.

Giardini PA, Fletcher DA, Theriot JA (2003). Compression forces generated by actin comet tails on lipid vesicles. Proc Natl Acad Sci USA 100, 6493–6498.

Gov N (2018). Guided by curvature: shaping cells by coupling curved membrane proteins and cytoskeletal forces. Phil Trans R Soc B 373, 20170115.

Guven J (2004). Membrane geometry with auxiliary variables and quadratic constraints. J Phys A: Math Gen 37, L313.

Hassinger JE, Oster G, Drubin DG, Rangamani P (2017). Design principles for robust vesiculation in clathrin-mediated endocytosis. Proc Natl Acad Sci USA 114, E1118–E1127.

Heinrich V, Božič B, Svetina S, Žekš B (1999). Vesicle deformation by an axial load: from elongated shapes to tethered vesicles. Biophys J 76, 2056–2071.

Helfrich W (1973). Elastic properties of lipid bilayers: theory and possible experiments. Z Naturforsch C 28, 693–703.

Hochmuth RM (2000). Micropipette aspiration of living cells. J Biomech 33, 15–22.

Holzapfel GA, Eberlein R, Wriggers P, Weizsäcker HW (1996). Large strain analysis of soft biological membranes: formulation and finite element analysis. Comput Meth Appl Mech Eng 132, 45–61.

Iglič A, Hägerstrand H, Veranič P, Plemenitaš A, Kralj-Iglič V (2006). Curvature-induced accumulation of anisotropic membrane components and raft formation in cylindrical membrane protrusions. J Theor Biol 240, 368–373.

Jenkins J (1977). Static equilibrium configurations of a model red blood cell. J Math Biol 4, 149–169.

Jin AJ, Prasad K, Smith PD, Lafer EM, Nossal R (2006). Measuring the elasticity of clathrin-coated vesicles via atomic force microscopy. Biophys J 90, 3333–3344.

Karotki L, Huiskonen JT, Stefan CJ, Ziółkowska NE, Roth R, Surma MA, Krogan NJ, Emr SD, Heuser J, Grünewald K, Walther TC (2011). Eisosome proteins assemble into a membrane scaffold. J Cell Biol 195, 889–902.

Kirchhausen T (2012). Bending membranes. Nat Cell Biol 14, 906.

Kishimoto T, Sun Y, Buser C, Liu J, Michelot A, Drubin DG (2011). Determinants of endocytic membrane geometry, stability, and scission. Proc Natl Acad Sci USA 108, E979–E988.

Kozlov MM, Campelo F, Liska N, Chernomordik LV, Marrink SJ, McMahon HT (2014). Mechanisms shaping cell membranes. Curr Opin Cell Biol 29, 53–60.

Kukulski W, Schorb M, Kaksonen M, Briggs JA (2012). Plasma membrane reshaping during endocytosis is revealed by time-resolved electron tomography. Cell 150, 508–520.

Kuzmin PI, Akimov SA, Chizmadzhev YA, Zimmerberg J, Cohen FS (2005). Line tension and interaction energies of membrane rafts calculated from lipid splay and tilt. Biophys J 88, 1120–1133.

Lee H, Pastor RW (2011). Coarse-grained model for PEGylated lipids: effect of PEGylation on the size and shape of self-assembled structures. J Phys Chem B 115, 7830–7837.

Lee HJ, Peterson EL, Phillips R, Klug WS, Wiggins PA (2008). Membrane shape as a reporter for applied forces. Proc Natl Acad Sci USA 105, 19253–19257.

Lee LM, Liu AP (2014). The application of micropipette aspiration in molecular mechanics of single cells. J Nanotechnol Eng Med 5, 0408011.

Lee MC, Orci L, Hamamoto S, Futai E, Ravazzola M, Schekman R (2005). Sar1p n-terminal helix initiates membrane curvature and completes the fission of a COPII vesicle. Cell 122, 605–617.

Lim SK, Wong AS, de Hoog H-PM, Rangamani P, Parikh AN, Nallani M, Sandin S, Liedberg B (2017). Spontaneous formation of nanometer scale tubular vesicles in aqueous mixtures of lipid and block copolymer amphiphiles. Soft Matter 13, 1107–1115.

Lingwood D, Simons K (2010). Lipid rafts as a membrane-organizing principle. Science 327, 46–50.

Lipowsky R (1992). Budding of membranes induced by intramembrane domains. J Phys II 2, 1825–1840.

Lipowsky R (1995). Bending of membranes by anchored polymers. Europhys Lett 30, 197.

Lipowsky R (2013). Spontaneous tubulation of membranes and vesicles reveals membrane tension generated by spontaneous curvature. Faraday Discuss 161, 305–331.

Liu J, Kaksonen M, Drubin DG, Oster G (2006). Endocytic vesicle scission by lipid phase boundary forces. Proc Natl Acad Sci USA 103, 10277–10282.

Lokar M, Kabaso D, Resnik N, Sepčić K, Kralj-Iglič V, Veranič P, Zorec R, Iglič A (2012). The role of cholesterol-sphingomyelin membrane nanodomains in the stability of intercellular membrane nanotubes. Int J Nanomed 7, 1891.

Lučić V, Rigort A, Baumeister W (2013). Cryo-electron tomography: the challenge of doing structural biology in situ. J Cell Biol 202, 407–419.

Mattila PK, Lappalainen P (2008). Filopodia: molecular architecture and cellular functions. Nat Rev Mol Cell Biol 9, 446–454.

McDargh ZA, Vázquez-Montejo P, Guven J, Deserno M (2016). Constriction by dynamin: elasticity versus adhesion. Biophys J 111, 2470–2480.

McMahon HT, Gallop JL (2005). Membrane curvature and mechanisms of dynamic cell membrane remodelling. Nature 438, 590.

Mesarec L, Gozdz W, Iglivc S, Kralj V, Iglivc A (2016). Closed membrane shapes with attached bar domains subject to external force of actin filaments. Colloids Surf B 141, 132–140.

Mofrad MR, Kamm RD (2009). Cellular Mechanotransduction: Diverse Perspectives from Molecules to Tissues, New York: Cambridge University Press.

Monzel C, Sengupta K (2016). Measuring shape fluctuations in biological membranes. J Phys D: Appl Phys 49, 243002.

Mozdy A, McCaffery J, Shaw J (2000). Dnm1p gtpase-mediated mitochondrial fission is a multi-step process requiring the novel integral membrane component fis1p. J Cell Biol 151, 367–380.

Mukherjee S, Maxfield FR (2000). Role of membrane organization and membrane domains in endocytic lipid trafficking. Traffic 1, 203–211.

Naghdi PM (1973). The theory of shells and plates. In Linear Theories of Elasticity and Thermoelasticity, Berlin: Springer, 425–640.

Neves SR, Tsokas P, Sarkar A, Grace EA, Rangamani P, Taubenfeld SM, Alberini CM, Schaff JC, Blitzer RD, Moraru II, et al. (2008). Cell shape and negative links in regulatory motifs together control spatial information flow in signaling networks. Cell 133, 666–680.

Nickels JD, Chatterjee S, Stanley CB, Qian S, Cheng X, Myles DA, Standaert RF, Elkins JG, Katsaras J (2017). The in vivo structure of biological membranes and evidence for lipid domains. PLoS Biol 15, e2002214.

Phillips R, Kondev J, Theriot J, Garcia H (2012). Physical Biology of the Cell, New York: Garland Science.

Picco A, Mund M, Ries J, Nedelec F, Kaksonen M (2015). Visualizing the functional architecture of the endocytic machinery. Elife 4, e04535.

Powers TR, Huber G, Goldstein RE (2002). Fluid-membrane tethers: minimal surfaces and elastic boundary layers. Phys Rev E: Stat Phys, Plasmas, Fluids 65, 041901.

Prévost C, Tsai F, Bassereau P, Simunovic M (2017). Pulling membrane nanotubes from giant unilamellar vesicles. J Vis Exper 12, 1–9.

Rangamani P, Benjamini A, Agrawal A, Smit B, Steigmann DJ, Oster G (2014a). Small scale membrane mechanics. Biomech Model Mechanobiol 13, 697–711.

Rangamani P, Lipshtat A, Azeloglu EU, Calizo RC, Hu M, Ghassemi S, Hone J, Scarlata S, Neves SR, Iyengar R (2013). Decoding information in cell shape. Cell 154, 1356–1369.

Rangamani P, Mandadap KK, Oster G (2014b). Protein-induced membrane curvature alters local membrane tension. Biophys J 107, 751–762.

Richmond DL, Schmid EM, Martens S, Stachowiak JC, Liska N, Fletcher DA (2011). Forming giant vesicles with controlled membrane composition, asymmetry, and contents. Proc Natl Acad Sci USA 108, 9431–9436.

Robinson DG, Brandizzi F, Hawes C, Nakano A (2015). Vesicles versus tubes: is endoplasmic reticulum-Golgi transport in plants fundamentally different from other eukaryotes? Plant Physiol 168, 393–406.

Römer W, Berland L, Chambon V, Gaus K, Windschiegl B, Tenza D, Aly MR, Fraisier V, Florent J-C, Perrais D, et al. (2007). Shiga toxin induces tubular membrane invaginations for its uptake into cells. Nature 450, 670.

Roux A, Cappello G, Cartaud J, Prost J, Goud B, Bassereau P (2002). A minimal system allowing tubulation with molecular motors pulling on giant liposomes. Proc Natl Acad Sci USA 99, 5394–5399.

Roux A, Cuvelier D, Nassoy P, Prost J, Bassereau P, Goud B (2005). Role of curvature and phase transition in lipid sorting and fission of membrane tubules. EMBO J 24, 1537–1545.

Seifert U (1997). Configurations of fluid membranes and vesicles. Adv Phys 46, 13–137.

Semrau S, Schmidt T (2009). Membrane heterogeneity—from lipid domains to curvature effects. Soft Matter 5, 3174–3186.

Sens P, Plastino J (2015). Membrane tension and cytoskeleton organization in cell motility. J Phys: Condens Matter 27, 273103.

Shi Z, Graber ZT, Baumgart T, Stone HA, Cohen AE (2018). Cell membranes resist flow. bioRxiv 290643.

Shlomovitz R, Gov NS, Roux A (2011). Membrane-mediated interactions and the dynamics of dynamin oligomers on membrane tubes. New J Phys 13, 065008.

Simunovic M, Manneville J-B, Renard H-F, Evergren E, Raghunathan K, Bhatia D, Kenworthy AK, Voth GA, Prost J, McMahon HT, *et al.* (2017). Friction mediates scission of tubular membranes scaffolded by bar proteins. Cell 170, 172–184.

Smith A-S, Sackmann E, Seifert U (2004). Pulling tethers from adhered vesicles. Phys Rev Lett 92, 208101.

Snead WT, Hayden CC, Gadok AK, Zhao C, Lafer EM, Rangamani P, Stachowiak JC (2017). Membrane fission by protein crowding. Proc Natl Acad Sci USA 114, E3258–E3267.

Stachowiak JC, Schmid EM, Ryan CJ, Ann HS, Sasaki DY, Sherman MB, Geissler PL, Fletcher DA, Hayden CC (2012). Membrane bending by protein–protein crowding. Nat Cell Biol 14, 944–949.

Steigmann D (1999). Fluid films with curvature elasticity. Arch Ration Mech Anal 150, 127–152.

Steigmann D, Baesu E, Rudd RE, Belak J, McElfresh M (2003). On the variational theory of cell-membrane equilibria. Interface Free Bound 5, 357–366.

Steinkühler J, Różycki B, Alvey C, Lipowsky R, Weikl TR, Dimova R, Discher DE (2018). Membrane fluctuations and acidosis regulate cooperative binding of "marker of self" cd47 with macrophage checkpoint receptor sirpα. J Cell Sci 131, 1–27.

Stephens DJ, Allan VJ (2003). Light microscopy techniques for live cell imaging. Science, 300, 82–86.

Sydor AM, Czymmek KJ, Puchner EM, Mennella V (2015). Super-resolution microscopy: from single molecules to supramolecular assemblies. Trends Cell Biol 25, 730–748.

Tian A, Johnson C, Wang W, Baumgart T (2007). Line tension at fluid membrane domain boundaries measured by micropipette aspiration. Phys Rev Lett 98, 208102.

Todhunter I (1886). A History of the Theory of Elasticity and of the Strength of Materials: Galilei to Saint-Venant, 1639–1850. Vol. 2, Parts 1–2, Saint-Venant to Lord Kelvin, New York: Cambridge University Press.

Varma A, Morbidelli M, Wu H (2005). Parametric Sensitivity in Chemical Systems, New York: Cambridge University Press.

Veldhuis JH, Mashburn D, Hutson MS, Brodland GW (2015). Practical aspects of the Cellular Force Inference Toolkit (CellFIT). Methods Cell Biol 125, 331–351.

Walani N, Torres J, Agrawal A (2015). Endocytic proteins drive vesicle growth via instability in high membrane tension environment. Proc Natl Acad Sci USA 112, E1423–E1432.

Wäldchen S, Lehmann J, Klein T, Van De Linde S, Sauer M (2015). Light-induced cell damage in live-cell super-resolution microscopy. Sci Rep 5, 15348.

Waugh RE (1982). Surface viscosity measurements from large bilayer vesicle tether formation. II. Experiments. Biophys J 38, 29–37.

Zhao H, Michelot A, Koskela E, Tkach V, Stamou D, Drubin D, Lappalainen P (2013). Membrane sculpting BAR domains generate stable lipid microdomains. Cell Rep 4, 1213–1223.